

Pressure-Driven Explosive Energy Conversion in Lead-Free Ferroelectric (Ag, K)NbO₃

Kai Dai (戴凯),¹ Anyang Cui (崔安阳)^{1,*} Zhen Liu (刘振),² Li Chen (陈立),¹ Yuting Yan (严雨婷),¹ Lichen Gao (高立宸),¹ Kai Jiang (姜凯)¹, Jinzhong Zhang (张金中),¹ Yawei Li (李亚巍)¹, Genshui Wang (王根水),² Xianlin Dong (董显林),² and Zhigao Hu (胡志高)^{1,3,†}

¹Department of Physics, School of Physics and Electronic Science, Technical Center for Multifunctional Magneto-Optical Spectroscopy (Shanghai), Engineering Research Center of Nanophotonics & Advanced Instrument (Ministry of Education), East China Normal University, Shanghai 200241, China

²Key Laboratory of Inorganic Functional Materials and Devices, Shanghai Institute of Ceramics, Chinese Academy of Sciences, Shanghai 200050, China

³Collaborative Innovation Center of Extreme Optics, Shanxi University, Taiyuan, Shanxi 030006, China

(Received 25 August 2022; revised 2 March 2023; accepted 25 April 2023; published 17 May 2023)

Designing the giant-performance explosive energy conversion of lead-free ferroelectrics attracts increasing attention from the medical, energy, defense, and mining industries, whereas the underlying physics mechanism remains ambiguous. Here, chemical modification and pressure engineering are utilized to induce a structural competition between polar and nonpolar structures to achieve a superior explosive energy conversion (34.57 J/cm^3) from lead-free $(\text{Ag}_{0.935}\text{K}_{0.065})\text{NbO}_3$ ceramics, enabling a sharp mechanical-stimulating pulse current within microseconds and having excellent thermal stability of phase structure. We reveal that these merits are related to a local structural heterogeneity on the atomic length scale. Pressure-regulating ferroelectric-antiferroelectric order is responsible for its explosive energy conversion, in which the evolution of oxygen octahedron distortion and electronic transition dynamics under the stress field have been specified. This work reveals the physical origin of the excellent energy-conversion performance of $(\text{Ag}, \text{K})\text{NbO}_3$, and draws a clear scenario for developing the advanced lead-free ferroelectrics device with high-performance energy conversion.

DOI: 10.1103/PhysRevApplied.19.054058

I. INTRODUCTION

Recently, explosive or pulse-power energy-conversion property is of high interest under the global background of the high demand of energy. Ferroelectric materials are widely used in energy conversion, whose performance can be modulated by external (thermal, electrical, and mechanical) fields [1,2]. One case is that ferroelectric ceramics would depolarize and ultrafastly release the bound charge to generate an electrical current under the pressure control [3,4]. This depolarization behavior belongs to the force-electric effect, where the charge storage and release is determined by polar-nonpolar structure transformation or polarization switching [5–7]. The force-electric effect has been found in lead-based ferroelectric materials, and contributes to the development of high-power applications [8–11]. However, explaining the origin of the induced depolarization in microseconds is still challenging during the shock compression. Ferroelectric domain switch

and phase transition involving ferroelectric-paraelectric (FE-PE) order and ferroelectric-antiferroelectric (FE-AFE) order are mainly dominant under the compression [9, 12–15]. Since the FE-AFE transformation can be triggered at a lower pressure, the $\text{Pb}(\text{Zr}_{1-x}\text{Ti}_x)\text{O}_3$ (PZT) considered to be one of the best choices for explosive energy-conversion devices [15–17]. However, the stringent environmental regulation of lead toxicity limits PZT application. Therefore, it is urgent to develop a lead-free material alternative with the great-performance energy conversion.

In the ferroelectric system, constructing the adjacent phase boundaries is one of the most effective ways to improve the electromechanical coupling and energy-storage performances. Composition-related morphotropic phase boundary in Pb-based crystal causes the unstable polarization state and reduces energy barrier. Therefore, to build a high-performance lead-free energy-conversion material system, it requires that the structure should be located at the adjacent phase boundary. Recently, AgNbO_3 -based antiferroelectric ceramics have been proven to exhibit the promising energy storage or

*aycui@phy.ecnu.edu.cn

†zghu@ee.ecnu.edu.cn

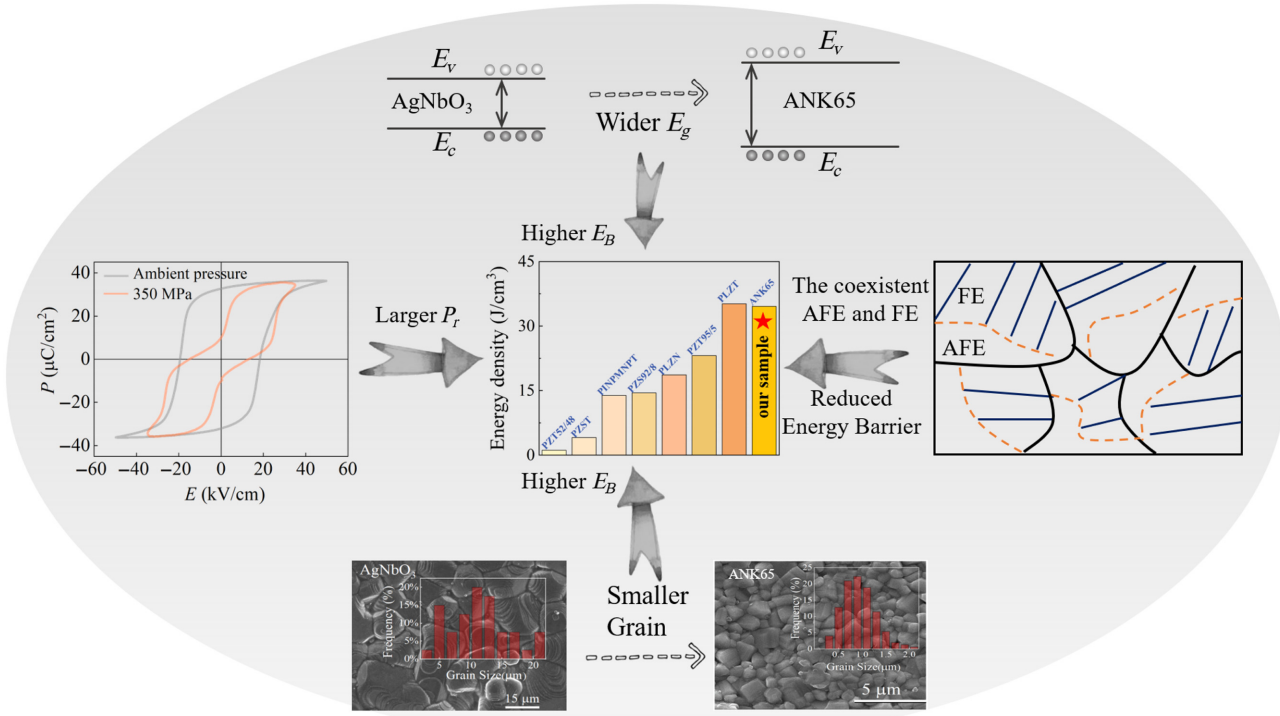


FIG. 1. Schematic diagram of an effective strategy for realizing high-performance explosive energy-conversion applications in AgNbO₃-based lead-free ceramics. A comparison of energy density with our work is shown among other bulk ceramics [7,9–11,13,14]. Polarization-electric field (P - E) loops are collected at ambient and 350-MPa pressure, respectively. E_c and E_v are represented to the conduction band and valence band, respectively.

conversion characteristics [14,18–22]. Doping engineering can reduce the gap of free energy from the anti-ferroelectric phase in pure AgNbO₃ to the ferroelectric phase, where the chemical doping can induce ferroelectricity by substituting cations of AgNbO₃, such as Li⁺ [23] and K⁺ [24,25]. The K⁺ modification can inhibit the oxygen octahedral tilt and enhance the ferroelectricity [24]. Fortunately, we find that lead-free K⁺-doped AgNbO₃ possesses an ultrahigh energy-storage density of 34.57 J/cm³ and a pulse current of approximately 22 A in 1.8 ms [14]. However, the underlying physical origin with the structure-performance relationship is still unclear, which hinders the further development of lead-free energy storage and conversion devices. Therefore, a more in-depth study is urgently required to reveal its physical origin and provide clear guidance for the design and optimization of high-performance lead-free energy-conversion ceramics.

Pressure is the key physical condition for the explosive energy-conversion application. Here, we designed a FE-AFE phase boundary in a 6.5% potassium cation modified AgNbO₃ (ANK65) to gain a high-performance energy-storage density of over 34.5 J/cm³. To guide its energy-conversion applications, an overall strategy has been summarized in Fig. 1, which needs to simultaneously

satisfy the following structural properties: larger remanent polarization (P_r) enhanced the energy-storage density; the wider band gap (E_g) and smaller crystalline grain improved the intrinsic breakdown strength (E_B); the coexistence of polar and nonpolar phase reduced FE-AFE energy barrier. Within the phase boundary, local structure heterogeneity and the coexistent polar ($Pmc2_1$) and nonpolar ($Pbcm$) orders have been observed on the atomic scale to the micrometer scale. Pressure- (up to 1260 MPa) induced transition mechanism is studied, which is accompanied by the oxygen octahedron distortion during the process of structural transformation. Our work further promotes the possibility of lead-free ceramics to replace PZT in explosive energy-conversion applications.

II. MATERIALS AND METHODS

ANK65 ceramic is prepared by the solid-state reaction method. The raw materials of Ag₂O (99.7%), Nb₂O₅ (99.93%), and K₂CO₃ (99.9%) are ball milled in ethanol for 12 h. The mixtures are calcined in oxygen atmosphere at 870 °C for 3 h. After calcination, the powder is ball milled again for 12 h and is compressed into 15-mm-diameter pellets with polyvinylalcohol as a binder. The

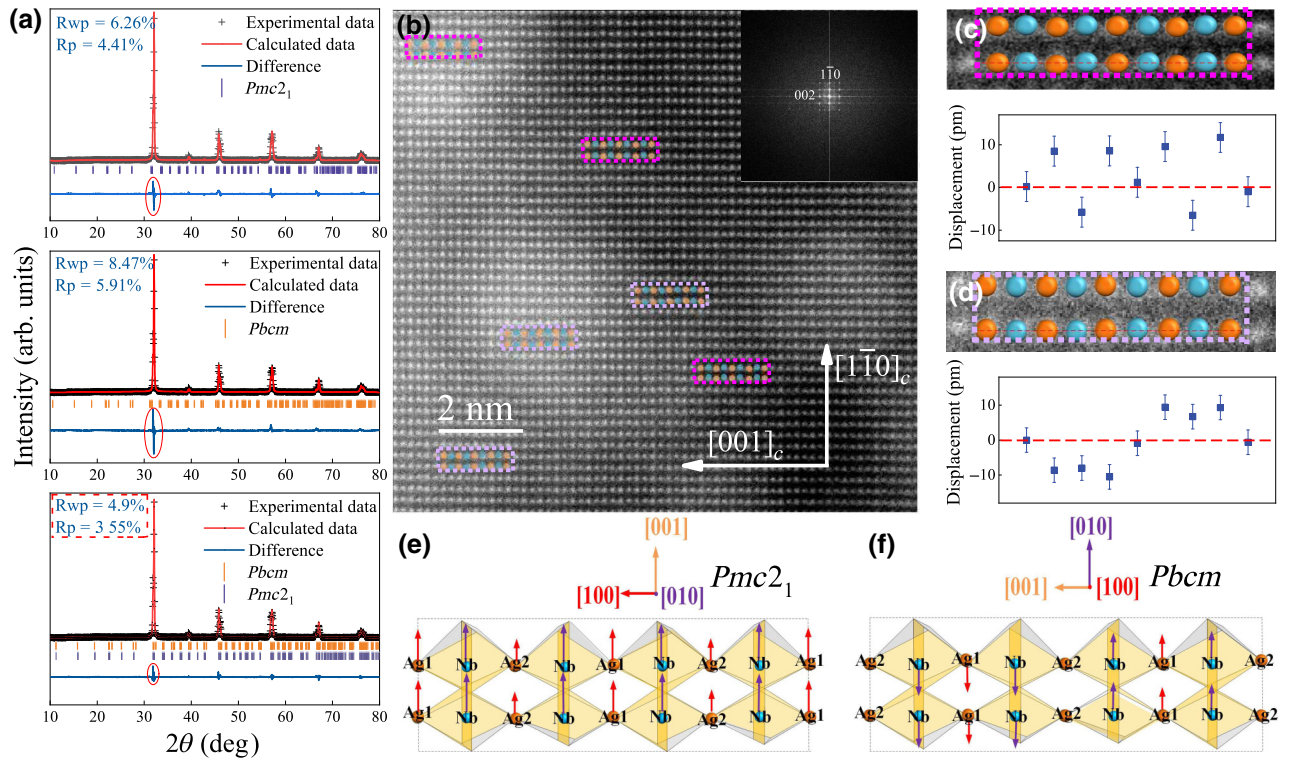


FIG. 2. (a) Rietveld refinement patterns of XRD for ANK65 in terms of $Pmc2_1$ model; $Pbcm$ model; two-phase model ($Pmc2_1 + Pbcm$). (b) The HAADF STEM image of ANK65 ceramic, while the illustration in the upper right corner is its fast Fourier transform. The magnified view of the (c) purple and (d) pink rectangular area in (b), and the measured cation displacement values. The orange spots and the blue spots represent Ag atoms and Nb atoms, respectively. The schematics of the displacements in the unit cell by (e) $Pmc2_1$ and (f) $Pbcm$. The relative cation displacement boxed by purple areas follows $Pmc2_1$ structure, while the pink areas are $Pbcm$ symmetry.

pellets are sintered at 1100 °C for 3 h. A flowing O₂ atmosphere is used to prevent the decomposition of silver oxide during the sintering process. The ceramic is polished to a thickness of 0.5 mm and a diameter of 8.0 mm. For electrical performance measurement, the silver electrodes are pasted on both sides of the ceramic and sintered at 700 °C for 0.5 h.

The structure of ANK65 powder sample are explored by x-ray diffraction (XRD) (Bruker D8 ADVANCE X), with a Cu K α rotating source. The STEM sample is prepared by a dual-beam focused ion beam (FIB) system (Nanolab Helios 650) using Ga ion accelerating voltage (30 kV). Next, an ion milling (Gatan 691) operation is implemented from 24 pA to 9.3 nA. The atomic resolution HAADF-STEM image is captured by the STEM mode of JEM Grand ARM300F microscope, which has double spherical aberration (Cs) correctors operating at 300 kV. The convergence angle of the probe is 24 mrad, while the detection angles are 63–180 mrad. The relative cation displacement is measured based on Gaussian fitting. The microstructure of ANK65 ceramic is characterized by field emission SEM (FEI Quanta 400 FEG, America).

The P - E loops are tested by an aixACCT TF 2000 analyzer FE measuring system (aixACCT Co., Aachen, Germany) at 1-Hz frequency. The morphology and ferroelectric domain structure of ANK65 ceramic are indicated by atomic force microscope (Dimension Icon, Bruker) and piezoresponce force microscope (PFM). The shock-wave compression experiment can be referred to Ref. [14].

Raman-scattering spectra are investigated by a micro-Raman spectrometer (Jobin-Yvon LabRAM HR Evolution, Horiba) with ultralow frequency accessory, while the frequency range of 5–1000 cm⁻¹. The laser with a wavelength of 532 nm is taken as the exciting source. For the *in situ* high-pressure Raman-scattering experiment, ANK65 ceramic is crushed into powders with sizes of a few microns. ANK65 powder and Ruby particles are put into a 100-μm-diameter hole, which are drilled in a 200-μm-thick tungsten gasket preretracted by a Mao Bell diamond anvil cell. *In situ* Raman-scattering measurements are performed at room temperature under the hydrostatic pressure of 0–1260 MPa, while the pressure transmission medium is silicone oil. The temperature-dependent experiments (−190 to 230 °C) are achieved by Linkam THMSE

TABLE I. The lattice parameters, phase fractions, atomic coordinates, and refinement reliability factors of refined $Pmc2_1$ and $Pbcm$ structure.

Space group:	$Pmc2_1$			phase fraction: 64.9%		
Lattice parameters:				$a = 7.8603 \text{ \AA}$	$b = 5.576 \text{ \AA}$	$c = 5.616 \text{ \AA}$
Atomic label	Occupancy	Wyckoff site	x	y	z	Biso (\AA^2)
Ag1	0.935	2a	0	0.7402	0	0.011
K1	0.065	2a	0	0.7402	0	0.011
Ag2	0.935	2b	0.5	0.7422	-0.0034	0.015
K2	0.065	2b	0.5	0.7422	-0.0034	0.015
Nb1	1	4c	0.752	0.2478	0.0144	0.012
O1	1	2a	0	0.7829	0.4668	0.01
O2	1	2b	0.5	0.71	0.4797	0.01
O3	1	4c	0.775	0.4723	0.2636	0.01
O4	1	4c	0.267	0.04	0.6974	0.01
Space group:	$Pbcm$			Phase fraction: 35.1%		
Lattice parameters:			$a = 5.534 \text{ \AA}$	$b = 5.683 \text{ \AA}$	$c = 15.764 \text{ \AA}$	
Atomic label	Occupancy	Wyckoff site	x	y	z	Biso (\AA^2)
Ag1	0.935	4c	-0.251	0.25	0	0.035
K1	0.065	4c	-0.251	0.25	0	0.035
Ag2	0.935	4d	-0.256	0.2428	0.25	0.022
K2	0.065	4d	-0.256	0.2428	0.25	0.022
Nb1	1	8e	0.246	0.2422	0.1256	0.011
O1	1	4c	0.302	0.25	0	0.017
O2	1	8e	-0.029	0.0303	0.114	0.022
O3	1	8e	0.5262	0.4778	0.1375	0.015
O4	1	4d	0.215	0.262	0.25	0.021

600 heating and cooling stage. The temperature effects are corrected by the Bose-Einstein factor coefficient [26] $n(\omega, T) = [\exp(\hbar\omega/kT) - 1]^{-1}$, where ω , T , \hbar , and k are phonon wave number, temperature, Planck constant, and Boltzmann constant, respectively.

SE measurements are examined by a visible-ultraviolet spectroscopic ellipsometer in the photon energy range of 230–1240 nm (1–5.4 eV) (V-VASE by J. A. Woolam Co., Inc.) with the spectral resolution of 5 nm, while the incident angle is fixed at 70°. The software package WVASE32 is used for analysis.

All calculations in this study are carried out by the Vienna *ab initio* simulation package (VASP) using the projector augmented wave (PAW) method and a plane-wave basis set. In order to have an insight into the electronic structure, the calculations are performed directly with the Heyd-Scuseria-Ernzerhof method. The electron interaction is employed along with a kinetic energy cutoff of 550 eV. The $4 \times 9 \times 3$ k -point sample selected by the Monkhorst-Pack method is used to describe the Brillouin zone. The structure of ANK65 can be indicated by antiferroelectric orthorhombic lattice in $Pbcm$ space group and ferroelectric orthorhombic lattice in $Pmc2_1$ space group. Structural optimizations are carried out in two structure and the ions are fully relaxed toward equilibrium until the residual forces on each atom are less than 0.02 eV/A, and the total energy convergence criterion is set as 10^{-5} eV.

III. RESULTS AND DISCUSSION

XRD patterns of ANK65 in Fig. 2(a) show the symmetry structures refined by the space groups of $Pbcm$, $Pmc2_1$, and the coexistent $Pbcm$ and $Pmc2_1$. In comparison with the structural models of nonpolar ($Pbcm$) and polar ($Pmc2_1$), the $Pbcm$ and $Pmc2_1$ coexistence matches the experimental data better, with the smallest weighted profile (R_{WP}) and profile reliability factors (R_p) of 4.9% and 3.55%, respectively. It confirms that the ANK65 sample would follow a structural competition between polar and nonpolar orders. Table I lists the detailed information about lattice parameters, phase fractions, atomic coordinates, and refinement reliability factors. The $Pmc2_1$ and $Pbcm$ mixture reduces the energy barrier of FE and AFE phase, which can trigger the force-electric effect.

Then, we employ atomical resolved high-angle annular dark-field scanning transmission electron microscopy (HAADF STEM) to observe the real structure of ANK65 crystal, as shown in Fig. 2(b), where HAADF is referred to as the Z-contrast image related to the atomic number of atoms [27]. Here, Ag has the largest atomic number among the four elements Ag (47), Nb (41), K (19), and O (8). Therefore, Ag columns appear as the brighter contrast, while Nb columns are slightly darker. Each cation deviates along different crystalline directions, forming a wavy atomic plane. To be more specific, Ag and Nb

TABLE II. The best-fitting parameters in the Tauc-Lorentz and Lorentz oscillator for SE at room temperature.

Sample	ε_∞	E_g (eV)	B_{r1}	E_{n1} (eV)	A_1	C_1	E_{n2} (eV)	A_2
Ambient pressure	1.72	3.07	3.37	4.45	209.5	5.89	3.36	0.23
After pressure loading	1.78	3.02	3.02	4.41	204.1	6.25	3.31	0.16

atoms displace along the $[1\bar{1}0]_c$ axis and fluctuate along $[001]_c$ -axis direction. Simultaneously, every four consecutive Ag-Nb pairs form a repeating unit, which reflects eight atoms in one fluctuation period. Two typical phase regions are magnified in Figs. 2(c) and 2(d), in which their ionic displacement are valued. It clearly shows local structure heterogeneity on ANK65 ceramic by examining the difference of these representative regions. Figures 2(e) and 2(f) show the structure with $Pmc2_1$ and $Pbcm$, where arrows emphasize the relative displacement and their difference of noncentrosymmetric ($Pmc2_1$) and central ($Pbcm$) space groups. The average displacement of Nb ions along $[001]$ axis in $Pmc2_1$ cells is much larger than that of Ag. Whereas the average displacement of Ag and Nb atoms along $[010]$ axis is relatively close in nonpolar $Pbcm$ cell, which corresponds to $[001]$ axis for $Pmc2_1$ cell [18,28,29]. Ag1 site has an equal antiparallel displacement along $[010]$ or $[\bar{0}10]$, while Ag2 site does not shift in $Pbcm$ cell. Similarly, four Nb^{5+} pairs present antiparallel displacements along $[010]$ or $[\bar{0}10]$ for $Pbcm$. In contrast, all the cations have a displacement along $[001]$ axis in $Pmc2_1$ cell, showing a larger net polarization along $[001]$ axis. We demonstrate that the relative cation displacements in two typical regions are consistent with the structure of $Pbcm$ and $Pmc2_1$ phase. Therefore, the STEM results provide direct evidence for the coexistence of polar ($Pmc2_1$) and nonpolar ($Pbcm$) phases.

Pressure-dependent ferroelectric hysteresis polarization-electric field (P - E) loops of ANK65 ceramic shown in the inset of Fig. 1 exhibit the P_r of $32 \mu\text{C}/\text{cm}^2$. The higher P_r presents more pulsed electrical power can be obtained, while the ferroelectricity is enhanced with the introduction of K^+ . Upon the compression at 350 MPa, the pinched loop still reveals the antiferroelectric hysteresis, although the presence of nonzero remnant polarization existed. The common belief that pinched loops derived from the presence of multiple domains and structural defects, such as domain walls being strongly pinned by charged defects. However, Xu *et al.* point that the pinched loops also exists in defect-free ferroelectric materials. The pinched loops may occur at morphotropic phase boundaries, while the free energy of ferroelectric and antiferroelectric ones are very close to each other [30]. Simultaneously, the ferroelectric phase on ANK65 ceramic is more sensitive to the applied pressure. Thus, as the pressure is increased to 350 MPa, the structure will change from the ferroelectric to

the antiferroelectric phase, while the existence of pinched loops is reasonable. Moreover, ANK60 ceramic shows similar results that there exists a decrease tendency for remnant polarization with the increasing pressure in our previous work [14]. Therefore, we believe the reason for the existence of pinched loops is the coexistence of FE and AFE phase. Meanwhile, we utilize PFM to image in-plane and out-of-plane spontaneous polarizations of ANK65 ceramic as the ferroelectric domains, showing domain size of hundreds of nanometers from Fig. 5. This is because structural competition of polar and nonpolar phase breaks long-range order, leading to the emergence of nanoscale domains [31–33]. Due to the structure not being recovered from the nonpolar $Pbcm$ phase to the initial polar $Pmc2_1$ with no external field, ANK65 ceramic can maintain antiferroelectric structure after withdrawal of the pressure. Therefore, ferroelectric domain after pressure loading is invisible for PFM.

The local structure heterogeneity is proven by the STEM results, while the microscopic electronic structure is intently related to superior properties. Therefore, pressure-dependent band gap and electronic transition behaviors are explored to reveal the explosive energy-conversion mechanism in ANK65 ceramic. By spectroscopic ellipsometry (SE), the dielectric functions ($\varepsilon = \varepsilon_1 + \varepsilon_2$) are determined by the nonlinear regression fitting method. A multilayer superposition model (air/rough/ANK65) is established to describe the sample structure, considering a rough surface measured in Fig. 6(a). The dielectric functions and E_g of ANK65 are obtained by the coupling of Tauc-Lorentz and Lorentz oscillator models, which can conform to Kramers-Kroning constraints. The best-fitting parameters are listed in Table II. Figures 3(a) and 3(b) show the experimental and fitting spectra at the wavelength range of 230–1240 nm, as well as the dielectric functions of ANK65 ceramic

TABLE III. Best fitting parameters of the SCP model for ANK65 ceramics.

Sample		A	ϕ (deg)	E (eV)	Γ (eV)
Ambient pressure	E_{cp1}	1.12	15.55	3.66	0.68
	E_{cp2}	3.32	41.1	4.78	1.37
After pressure loading	E_{cp1}	2.71	15.04	3.56	0.87
	E_{cp2}	0.88	40.1	4.30	0.87

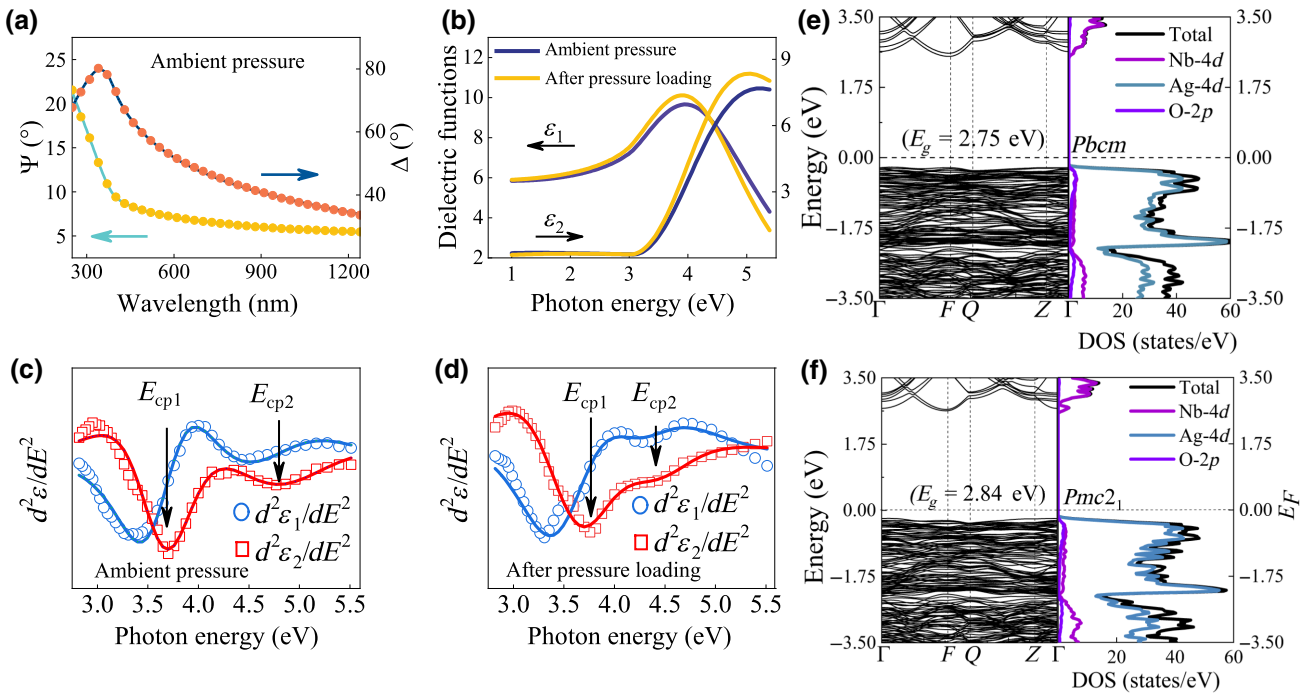


FIG. 3. (a) The experimental ellipsometric (dots) and the best fitting (solid lines) spectra of Psi (Ψ) and Delta (Δ) for ANK65. (b) The dielectric functions (ϵ_1 and ϵ_2) of ANK65 ceramic. The second derivatives of the dielectric functions spectra (dots) and the best-fitted spectra (solid lines) for ANK65 on the conditions of (c) ambient pressure (d) after pressure loading. Two interband transition E_{cp1} and E_{cp2} features are marked by arrows. Calculated band structure and corresponding density of states for (e) $Pbcm$, (f) $Pmc2_1$ phases of ANK65.

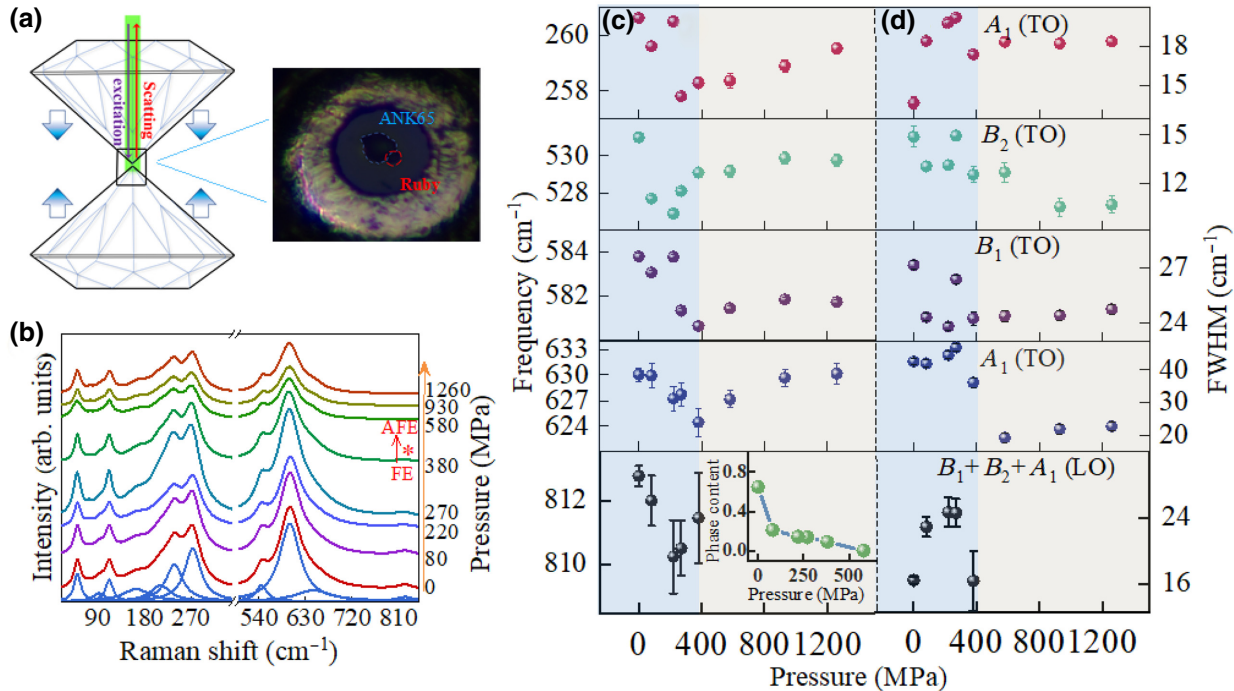


FIG. 4. (a) Schematic diagram of hydrostatic compression, in which the ANK65 powder and a ruby in a diamond anvil cell. (b) Pressure-dependent Raman spectra of ANK65. Bottom shows the corresponding multi-Lorentz fitting process at atmospheric pressure. (c) The frequency and (d) the FWHM evolution of main Raman-active phonon at 0–1260 MPa for ANK65. The two-phase ratios at different pressures is shown in the inset, while the ratio of the vertical axis is the $pmc2_1$ phase.

with the corresponding photon energy range of 1–5.4 eV. The imaginary part ε_2 of ANK65 ceramic is close to zero below the absorption edge, which indicates no additional electronic transition in the low-energy region. ε_2 sharply increases with further increasing photon energy, owing to the strong absorption, indicating the transition of interband electrons from valence-band maximum (VBM) to conduction-band minimum (CBM). SE results show that ANK65 has a wider E_g (about 3.07 eV) than pure AgNbO_3 (2.99 eV) at ambient pressure [34,35]. A wider E_g than pure AgNbO_3 means that it is hard to transition from the valence band to the conduction band for electrons, which contributes to higher E_B [36]. Simultaneously, the E_g of ANK65 after pressure loading decreases to about 3.02 eV. In addition, the electronic band structure observed in the dielectric spectra of ANK65 ceramic is attributed to interband transitions, while the standard critical point (SCP) model is performed to study the stress evolution of interband transitions [37]. The second derivative of ε_1 and ε_2 are displayed in Figs. 3(c) and 3(d), where the fitting parameters for the SCP model are summarized in Table III. The critical point $E_{\text{cp}1}$ is mainly dominated by *A*-site cation *d* orbital and oxygen anion *p* orbital, while $E_{\text{cp}2}$ is closely related to *B*-site cation *d* orbital [38]. The peak position of $E_{\text{cp}1}$ and $E_{\text{cp}2}$ shifts to the lower energy after pressure loading, whose trend is in agreement with the pressure-dependent evolution of E_g . Therefore, it provides a direct evidence that the wider band gap than pure AgNbO_3 meets the need of high explosive energy-conversion device in the given strategy (Fig. 1), while the pressure-induced structural transition for ANK65 is accompanied with the decrease of the band gap.

First-principles calculations are then carried out to reveal the band structure of ANK65 by studying orbital

hybridization and covalency [39], which can also, in conjunction with SE results, shed light on the physical mechanism of structural transformation [40,41]. It is well known for density functional theory (DFT) that the calculated band gap is underestimated by about 20%–30% compared with the experimental value due to the inherent of delocalization error and derivative discontinuity [42–44]. To eliminate the calculation error, the calculations based on the Heyd-Scuseria-Ernzerhof hybrid functional (HSE) are conducted to determine band gap. Its basic structure can be indicated by orthorhombic antiferroelectric ($Pbcm$) and ferroelectric ($Pmc2_1$) lattice. Figures 3(e) and 3(f) show the band structure and density of states (DOS) of ANK65 ceramics at different phases. The band structure of the antiferroelectric phase is generally close to that of ferroelectric phase, although the symmetry of the antiferroelectric phase is better than the ferroelectric one. Detailed analysis indicates that the interband transition mainly derives from $\text{O}-2p/\text{Ag}-4d$ to $\text{Nb}-4d$. The calculated band gap is indirect and the values are 2.75 and 2.84 eV for antiferroelectric and ferroelectric phases, respectively. The VBM is made up of $\text{O}-2p$ and $\text{Ag}-4d$ states, while the CBM is mainly composed of $\text{Nb}-4d$, and $\text{O}-2p$ states. Compare with some common niobates ($\text{KNbO}_3/\text{NaNbO}_3$), AgNbO_3 still exists some differences according to the effect of crystal field theory. The VBM are primarily constructed from the $\text{O}-2p$ states, while the CBM are dominated by the hybridization of $\text{Nb}-4d$ and $\text{O}-2p$ states on the $\text{KNbO}_3/\text{NaNbO}_3$ system. The electronic states of Na and K ions have little contribution to the valence and conduction bands, since the high ionicity of Na and K makes it difficult to form a covalent bond with other atoms by hybridization [45–47]. However, $\text{Ag}-4d$ contributes an essential role on the valence band according

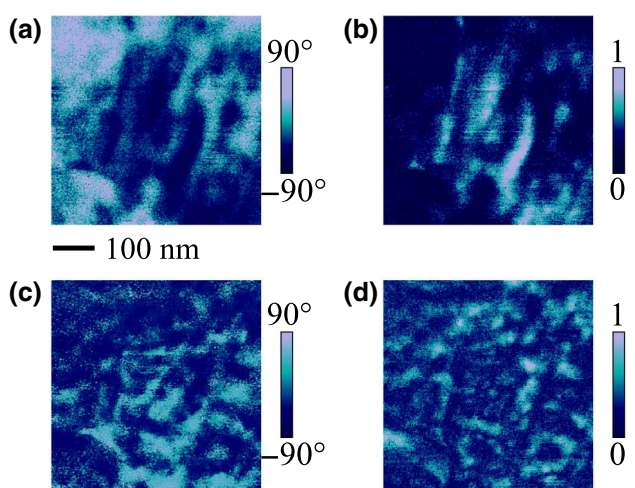


FIG. 5. The (a) out-of-plane phase, (b) out-of-plane amplitude, (c) in-plane phase, and (d) in-plane amplitude PFM images for ANK65 ceramic, respectively.

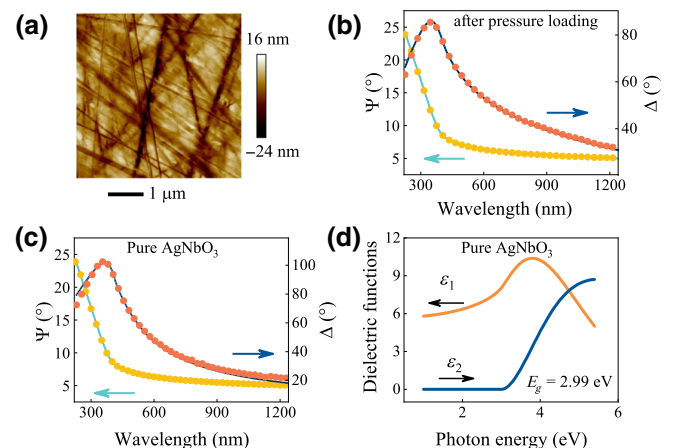


FIG. 6. (a) AFM topography of ANK65 ceramic. The experimental ellipsometric (dots) and the best-fitting (solid lines) spectra Ψ and Δ of (b) ANK65 after pressure loading and the pure AgNbO_3 at 300 K. (d) The dielectric functions (ε_1 and ε_2) of AgNbO_3 ceramics, while the band gap is 2.99 eV.

to the effect of crystal field theory. The inconsistent crystal structure leads to differences in the energy bands, while the investigation of difference in band gap is crucial for understanding phase transition. At the same time, the $Pbcm$ and $Pmc2_1$ space groups are relatively similar, thus the calculation and comparison of these two structures are very crucial to reveal the structure transformation mechanism of ANK65 ceramics. The antiferroelectric phase has lower E_g than the ferroelectric one, which is consistent with the SE results. The bonding and antibonding orbits, especially for Nb—O, approach with increasing the structural symmetry, corresponding to the weakening of orbital degeneracy [48]. Consequently, the ferroelectric phase ($Pmc2_1$) has a large Nb—O bond length than the antiferroelectric ($Pbcm$). Therefore, the band gap in the lower ferroelectric symmetry becomes wider than that of the antiferroelectric one, which confirms the interband transition behaviors from SE well.

Charge release process of ANK65 powder sample under pressure is determined by the polar to nonpolar phase transition, whose specific evolution is then explored by the confocal Raman spectra in the stress field of 0–1260 MPa. Figure 4(a) displays the schematic diagram of the hydrostatic compression measurement, while the ANK65 and a ruby are put in a diamond anvil cell. Group theory predicts that the lattice-vibrational irreducible Raman-active modes in $Pmc2_1$ and $Pbcm$ space group can be examined by $\Gamma_{Pmc2_1} = 16A_1 + 13A_2 + 12B_1 + 16B_2$ and $\Gamma_{Pbcm} = 15A_g + 17B_{1g} + 15B_{2g} + 13B_{3g}$ [49,50]. The representing Raman-active phonon is recognized from Raman spectra in Fig. 4(b), which are fitted by multi-Lorentzian oscillator. Scattering peaks at the frequency ranges of less than 130 cm^{-1} and $130\text{--}340\text{ cm}^{-1}$ are mainly related to the breathing modes of Ag^+ , K^+ , and the A_1 (TO) near 260 cm^{-1} , respectively [51], while high-frequency range of over 340 cm^{-1} corresponds to the vibration of oxygen octahedra including B_2 (TO) near 530 cm^{-1} , B_1 (TO) near 580 cm^{-1} , A_1 (TO) near 630 cm^{-1} , and $B_1 + B_2 + A_1$ (LO) near 810 cm^{-1} [52–54]. Figure 4(c) describes the pressure-dependent evolution of phonon frequency corresponding to the NbO_6 vibration. As pressure increases to 380 MPa, the phonon frequency moves to low-energy range as a red shift. Around 380 MPa as a critical pressure presents the anomalous peak shift, while the minimum is due to the flattening of the potential in the vicinity of a phase transition point, indicating the pressure-induced lattice transformation from polar structure ($Pmc2_1$) to the nonpolar ($Pbcm$) one [55,56]. The FWHM is also highly sensitive to the lattice structure, while the FWHM evolution of the oxygen octahedral phonon modes under pressure are shown in Fig. 4(d). It is noteworthy that the FWHM evolution with pressure also appears anomalous at the structure transition point. At the same time, some vibration modes annihilate in a highly symmetrical phase, such as the peak near the 810 cm^{-1} disappearance at pressure exceeding 380 MPa.

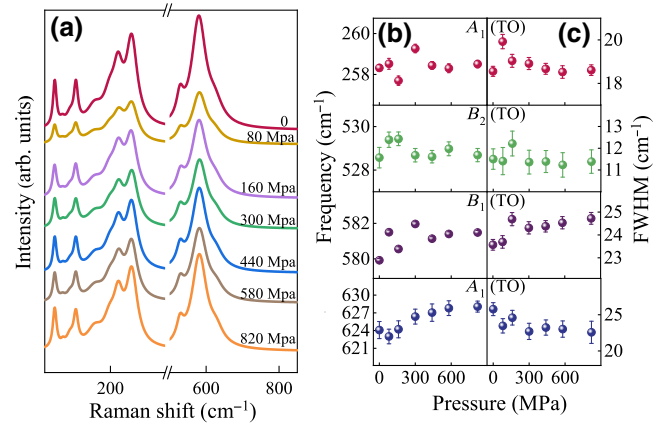


FIG. 7. Raman spectra of ANK65 on decompression. (b) The frequency and (c) the FWHM evolution of main Raman-active phonon at 820–0 MPa for decompression.

With increasing the hydrostatic pressure on ANK65, *in situ* neutron diffraction revealed the change of octahedral tilt from $a^-a^-c^+$ to $a^-a^-c^+/a^-a^-c^-$ by the annihilation of $1/2(321)_p$ and $1/2(341)_p$ superlattice peak [14]. Thus, the pressure induces a complete transformation from the ferroelectric $Pmc2_1$ phase to the antiferroelectric $Pbcm$ phase, while the transformation is accompanied by a change of the oxygen octahedral tilt. The high-pressure structure for ANK65 is a single phase with a stacking disorder along the c axis, consisting of alternating nanoregions of antiphase and in-phase tilts. The mixing of $Pbcm$ and $Pmc2_1$ phases is found in this study, while quantifying the amount of each phase with pressure is essential for the structure transition. Therefore, we assume a linear relationship between the intensity of $B_1 + B_2 + A_1$ (LO) phonons as a fraction of the highest intensity of the spectra and the structural transition process. The ANK65 powder sample is 35% $Pbcm$ as well as 65% $Pmc2_1$ at 0 MPa, while the structure is completely transformed to $Pbcm$ as the pressure is enhanced to 580 MPa. The intensity of all Raman signals is normalized to exclude the influence of external factors. We extract the intensities of $B_1 + B_2 + A_1$ (LO) phonons at different pressures, while the two-phase ratios are obtained at different pressures according to the two-phase occupancies at 0 and 580 MPa, as shown in the inset of the Fig. 4(c). The relieving pressure process is displayed in Fig. 7, while there is no phonon abnormal behavior during the pressure decreasing. These results indicate that the structure does not change from the $Pbcm$ to the $Pmc2_1$ phase as the pressure release.

Last but not least, let us follow the high-performance strategy of Fig. 1 to consider the polycrystalline microstructure and the better temperature stability of the ANK65 ceramic. Generally, ceramics are composed of randomly oriented anisotropic grains. SEM image on ANK65 ceramic shows the average grain size is about 1.02 μm ,

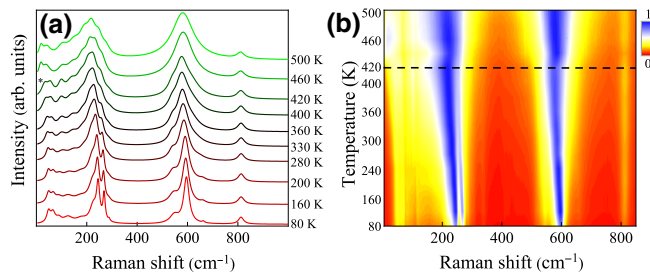


FIG. 8. Raman spectra of ANK65 on decompression. (b) The frequency and (c) the FWHM evolution of main Raman-active phonon at 820.0 MPa for decompression.

where the inset of the histogram shows the grain size complying with the normal distribution curve. The average grain size decreases obviously with the doping of potassium content [19,21,22,57]. On the one hand, the depleted space-charge layer appearing at the ceramic grain boundary would cause the larger resistivity, compared to the bulk resistivity. Smaller grain size means a large grain-boundary density and resistivity, greatly enhancing E_B . On the other hand, when hydrostatic pressure is applied, the stress distribution among the adjacent grains is complicated, where the neighboring grains with different orientations may clamp grains and hinder phase transition. More severely, the uneven grains and the increased local inhomogeneity will cause this effect to be more pronounced [15]. Therefore, the even and relatively small grain size on ANK65 ceramic promotes the energy-conversion performance. In addition, temperature stability is of great significance for designing the energy storage or conversion device. Figures 8(a) and 8(b) show the temperature-dependent Raman spectra of ANK65 ceramic at a wide temperature range of $-190\text{--}230^\circ\text{C}$. Although the Raman peaks are obviously broadened and smoothed as the temperature increases, the number of Raman peaks does not change, which shows that the local symmetry does not vary in a wider temperature range. The main phonon vibration modes all show a slight shift to a lower wave number and an increase in the FWHM. When the temperature exceeds 150°C , the expansion of cationic breathing mode indicates that the structural disorder increases and the polarity decreases. Therefore, we claim that ANK65 ceramic keeps a good temperature stability under 150°C , which can be used for energy device applications.

IV. CONCLUSION

As an alternative to traditional PZT material, a lead-free modified ANK65 ceramic is developed with a superior energy-conversion performance by constructing the pressure-driven FE-AFE phase boundary. The factors result in such a top performance, which are complex but have been summarized here into three key points: (i) the FE-AFE order mixture reduces the energy barrier

of FE and AFE phase; (ii) an increased electronic band gap enhances the breakdown strengths; (iii) a decrease in micrograin increases breakdown strengths and even grain distribution promotes the polar to nonpolar phase transition. Significantly, the physical origin of explosive energy conversion has been illustrated by specifying the FE-AFE phase boundary, electronic transition, and lattice dynamics under the stress field. The electronic structure of *Pbcm* and *Pmc2*₁ phases shows that its band gap of ANK65 is reduced after the irreversible phase transition under high pressure. Eventually, the designed ANK65 polycrystalline material is also proven to greatly satisfy the requirements about the ferroelectric hysteresis, the thermal stability of phase structure and the small micrograin size. The present work explores the origin of high explosive energy conversion on lead-free ferroelectric materials based on the in-depth understanding of lattice and electronic structure, and gives a distinct guide for future design of energy-conversion device.

ACKNOWLEDGMENTS

This work is financially supported by the National Natural Science Foundation of China (Grants No. 62090013, No. 12104156, No. 61974043, and No. 62074058), the National Key R&D Program of China (Grant No. 2019YFB2203403), the Projects of Science and Technology Commission of Shanghai Municipality (Grants No. 21JC1402100 and No. 19511120100), China Postdoctoral Science Foundation (Grants No. 2020TQ0099 and No. 2020M681222), the Program for Professor of Special Appointment (Eastern Scholar) at Shanghai Institutions of Higher Learning and Shanghai Pujiang Program (20PJ1403600).

APPENDIX A: THE DOPING STRATEGY AND THE MECHANISM OF PHASE COEXISTENCE

In the ferroelectric system, constructing the adjacent phase boundaries is one of the most productive ways to enhance the electromechanical coupling and the energy conversion performances. Therefore, the prerequisite of these candidate systems would be to possess a minor energy barrier between the FE and AFE phases. However, pure AgNbO₃ is the AFE-dominated ferrielectric phase, which has a weak ferroelectricity. Fortunately, the doping engineering can induce the transition of the structure from the AFE to the FE phase. The stability of the FE and AFE phase for the perovskite-type oxide is usually defined by the Goldschmid tolerance factor: $t = (R_A + R_O)/\sqrt{2}(R_B + R_O)$, where R_A, R_B, R_O refer to the average ionic radii of *A*-site cations, *B*-site cations, and oxygen anions. The AFE phase will be enhanced when $t < 1$, while the ferroelectricity will be strengthened when $t > 1$. Therefore, the FE phase can be induced by increasing the tolerance factor. The ionic radii of Ag⁺,

Nb^{5+} , and K^+ are 1.28 Å, 0.64 Å, and 1.64 Å, respectively. The larger K^+ ions will replace the smaller Ag^+ ions as the doping of the KNbO_3 , which will increase the tolerance factor and inhibit the tilting of the oxygen octahedra. Hence, the doping of K^+ will improve the stability of FE phase tremendously. Fu *et al.* pointed out that there exist three phase boundaries at $x_a \approx 0.07$, $x_b \approx 0.20$, and $x_c \approx 0.8$ on the $(\text{Ag}_{1-x}\text{K}_x)\text{NbO}_3$ (ANK) system [24]. When $x < x_a$, ANK will transition from the AFE-dominant AgNbO_3 -type orthorhombic ferrielectric phase to the orthorhombic phase that possesses strong ferroelectricity, while the ferroelectric structure is stabilized at $x_a < x < x_b$. When $x_b < x < x_c$, the structure of ANK single phase would not exist, while ANK will be transformed into the KNbO_3 -type orthorhombic structure when $x > x_c$. On this basis, the 6.5% component is located at the AFE and FE phase boundary exactly, while the structure can be refined to the coexisting of $Pbcm$ and $Pmc2_1$ phases [14]. According to the calculations from Niranjan *et al.*, the noncentrosymmetric ($Pmc2_1$) and centrosymmetric ($Pbcm$) structure of AgNbO_3 displays a slight energy difference (0.1 MeV/f.u.) [29], while both the FE and AFE order can coexist in ANK65 at room temperature. Simultaneously, the pressure-composition effect on the relative stabilities of the FE and AFE phases are studied in our previous work by the calculating the energy minimization, which matches perfectly with the structural analysis [14]. Therefore, the reason for phase coexistence in ANK65 is that the FE and AFE phase thermodynamic free-energy states are close.

APPENDIX B: THE FERROELECTRIC DOMAIN BEHAVIOR OF ANK65 CERAMICS

To further investigate the spontaneous polarization characteristics of ANK65 ceramics, the ferroelectric domain is mapped by PFM, where an alternating voltage is applied between tip and bottom electrodes in contact mode. The in-plane and out-of-plane domain images can be attained. As we know, the mostly orthorhombic crystals allow 12 possible polarization vectors in all [110], forming 60°, 90°, 120° or 180° domain-wall configurations [38]. The orientation types of the domain wall are mainly determined by the real symmetry of the crystalline phase, while the spontaneous polarization of orthorhombic crystalline is along the face diagonal of the original cubic unit cell. However, the lattice parameters of AgNbO_3 on the a axis are larger than those on the b axes or c axes (detailed lattice parameters are also listed in Table I), which causes the angle change of spontaneous polarization on adjacent domains. Therefore, in orthorhombic AgNbO_3 , the 60° and 120° domain wall will change to other angles. Phase contrast represented in the opposite polarization shows a clear domain with the size of several hundred nanometers, as shown in Figs. 5(a) and 5(c). The domain-wall structure could be displayed in

the amplitude channel, in which the piezoelectric response will offset to zero, as shown in Figs. 5(b) and 5(d). The PFM results avoid the interference of surface morphology.

APPENDIX C: THE OPTICALLY ELECTRONIC TRANSITIONS OF ANK65 CERAMICS

The study of optical transition is explored by spectroscopic ellipsometry (SE), which is significant to reveal the inherent physical mechanism of ANK65 ceramic. In the ellipsometry analysis, a multilayer superposition model (Air/Rough/ANK65) is built to depict the sample structure of ANK65 ceramic, considering the sample has a relatively rough surface displayed in Fig. 6(a). In addition, the rough layer is represented by the Bruggeman effective medium model with air and ANK65 accounting for half, respectively. The dielectric functions of the ANK65 layer are parameterized by the coupling of Tauc-Lorentz (TL) and Lorentz oscillator models, which can conform to Kramers-Kroning constraints. TL oscillator defines the E_g , and the excellent fitting result can be obtained by adding a Lorentz oscillator. The Lorentz oscillator is located above E_g , indicating the band-to-band transition.

The expression of the TL oscillator can be given

$$\begin{aligned} \varepsilon_1(E) &= \varepsilon_\infty + \frac{(2/\pi)P \int_{E_g}^\infty (\xi \pi \varepsilon_2(\xi))}{\xi^2 - E^2} d\xi, \\ \varepsilon_2(E) &= \frac{AE_n C (E - E_g)^2}{(E^2 - E_n^2)^2 + C^2 E^2} \frac{1}{E} (E \geq E_g), \\ \varepsilon_2(E) &= 0 (E < E_g). \end{aligned}$$

The parameters P , ε_∞ , E are the Cauchy principal part of integral, the high-frequency dielectric constant, and the incident photon energy, while the E_n , E_g , A , and C refer to the peak position energy, optical band gap, amplitude, and broadening term, respectively.

The expression of the Lorentz oscillator is

$$\varepsilon = \varepsilon_1 + i\varepsilon_2 = \varepsilon_\infty + \sum_{n=1}^j \frac{A_j}{E_{nj}^2 - E_n^2 + ib_{nj}E_n}.$$

The parameters A , b_r , E_n , j are the amplitude, the damping coefficient, the energy, and the number of oscillators, respectively. Correspondingly, the band structure observed in the dielectric spectra of ANK65 ceramic are originated from the interband transition, which can be evaluated based on the standard critical point mode (SCP). Notably, the surface roughness layer does not affect electronic transitions derived from the second partial derivative of dielectric functions basically. Therefore, the second derivative of complex dielectric functions are directly calculated by the original data. The second derivative of ε_1 and ε_2 of ANK65 ceramic (point) and fitting curve (solid line) are

displayed in Figs. 3(c) and 3(d). The position of critical point is expressed by an arrow and marked as E_{cp_1} and E_{cp_2} in order of photon energy from small to large.

The SCP model can be given by

$$\frac{d^2\varepsilon}{dE^2} = n(n-1)A_m e^{i\phi_m} (E - E_m + i\Gamma_m)^{n-2}, \quad n \neq 0,$$

$$\frac{d^2\varepsilon}{dE^2} = A_m e^{i\phi_m} (E - E_m + i\Gamma_m)^{-2}, \quad n = 0,$$

where m represents the m th vibrator, A_m , E_m , Γ_m , and ϕ_m are the amplitude, threshold energy, broadening, and phase angle. The value of n for exciton, one-dimensional, two-dimensional, and three-dimensional critical points are -1 , -0.5 , 0 , and 0.5 , respectively. Here, we fit the real and imaginary parts by exciton mode. The value of phase angle ϕ_m for two oscillators are between 0° and 90° , which conforms to the exciton deformation of critical point line shape [58].

APPENDIX D: DISCUSSION OF THE REASONS FOR IRREVERSIBLE AND REVERSIBLE STRUCTURAL TRANSFORMATION

The tilt-related pressure- and temperature-driven phase transition is fully reversible normally [59]. However, ANK65 has not returned to the initial FE phase even when released to ambient pressure, while the tilt of the oxygen octahedron changes significantly after the structural transition. Interestingly, a similar situation occurs in Nb-doped and La-doped PZT ceramics [15,60]. $Pb_{0.99}(Zr_{0.95}Ti_{0.05})_{0.98}Nb_{0.02}O_3$ have been investigated by Maxim Avdeev etc. in the range of hydrostatic pressure 0–600 Mpa, while the structure will transit from the rhombohedral $R3c$ to the antiferroelectric orthorhombic $Pbam$ phase. The structure transition is also accompanied by a change in the tilt of the octahedron, while the structure cannot recover to $R3c$ after pressure release. Avdeev claims that the stress or strain induced by the $Pbam$ phase prevents the atomic complete return to the beginning atomic positions as the pressure is released. It is interesting to note that the complete recovery of the $R3c$ phase needs to be achieved by heating the ceramic above 350 K, i.e., to the FR (HT) phase, and then reducing the temperature to room temperature. Similarly, we perform PE test for the sample after loading under an electric field, which finds the structure exhibited ferroelectric behavior. The evidence from neutron diffraction pattern, SE, PFM, Raman is inconsistent with the results of PE. However, we consider it reasonable for this situation, while the $Pbcm$ phase is a substable state at atmospheric pressure for ANK65. The exploration of the neutron diffraction pattern, SE, PFM, and Raman indicates that the structure could not be recovered from the $Pbcm$ phase to the initial $Pmc2_1$ with no external field, while the electric field induced the atoms to return to the

starting atomic position completely. Therefore, the stress or strain induced by the $Pbcm$ phase prevents the atomic complete return to the beginning atomic positions could be the reason for the metastable $Pbcm$ phase.

-
- [1] Z. Yang, H. L. Du, L. Jin, and D. Poelman, High-performance lead-free bulk ceramics for electrical energy storage applications: Design strategies and challenges, *J. Mater. Chem. A* **9**, 18026 (2021).
 - [2] L. L. Altgilbers, Explosive pulsed power: An enabling technology altgilbers, *Acta Phys. Pol. A* **115**, 1040 (2009).
 - [3] R. K. Linde, Depolarization of ferroelectrics at high strain rates Linde, *J. Appl. Phys.* **38**, 4839 (1967).
 - [4] V. N. Zubarev, Impact compression of piezoceramics Zubarev, *J. Appl. Mech. Tech. Phys.* **12**, 263 (1971).
 - [5] D. Berlincourt, H. Jaffe, H. H. A. Krueger, and B. Jaffe, Release of electric energy in $PbNb(Zr, Ti, Sn)O_3$ by temperature and by pressure enforced phase transitions, *Appl. Phys. Lett.* **3**, 90 (1963).
 - [6] Z. P. Gao, W. Peng, B. Chen, S. A. T. Redfern, K. Wang, B. J. Chu, Q. He, Y. Sun, X. F. Chen, H. C. Nie, W. Deng, L. K. Zhang, H. L. He, G. S. Wang, and X. L. Dong, Giant power output in lead-free ferroelectrics by shock-induced phase transition, *Phys. Rev. M* **73**, 035401 (2019).
 - [7] M. Xie, H. C. Nie, G. S. Wang, and X. L. Dong, Enhanced pressure-driven force-electric conversion effect for $(Pb, La)(Zr, Ti)O_3$ ferroelectric ceramics, *J. Am. Ceram. Soc.* **105**, 1210 (2021).
 - [8] P. C. Lysne, Shock induced polarization of a ferroelectric ceramic Lysne, *J. Appl. Phys.* **48**, 1024 (1977).
 - [9] S. I. Shkuratov, J. Baird, V. G. Antipov, W. Hackenberger, J. Luo, S. J. Zhang, C. S. Lynch, J. B. Chase, H. R. Jo, and C. C. Roberts, Complete stress-induced depolarization of relaxor ferroelectric crystals without transition through a nonpolar phase Shkuratov, *Appl. Phys. Lett.* **112**, 122903 (2018).
 - [10] N. B. Feng, H. C. Nie, X. F. Chen, G. S. Wang, X. L. Dong, and H. L. He, Depoling of porous $Pb_{0.99}(Zr_{0.95}Ti_{0.05})_{0.98}Nb_{0.02}O_3$ ferroelectric ceramics under shock wave load, *Curr. Appl. Phys.* **10**, 1387 (2010).
 - [11] S. I. Shkuratov, J. Baird, V. Antipov, E. Talantsev, J. Chase, W. Hackenberger, J. Luo, H. R. Jo, and C. Lynch, Ultrahigh energy density harvested from domain-engineered relaxor ferroelectric single crystals under high strain rate loading, *Sci. Rep.* **7**, 46758 (2017).
 - [12] K. H. Cho, E. S. Chang, Y. S. Choi, Y. H. Ko, and K. J. Kim, Effect of pressure on electric generation of PZT(30/70) and PZT(52/48) ceramics near phase transition pressure, *J. Eur. Ceram. Soc.* **32**, 457 (2012).
 - [13] H. R. Jo and C. S. Lynch, Effect of composition on the pressure-driven ferroelectric to antiferroelectric phase transformation behavior of $(Pb_{0.97}La_{0.02})(Zr_{1-x} - ySn_xTi_y)O_3$ ceramics, *J. Appl. Phys.* **116**, 074107 (2014).
 - [14] Z. Liu, T. Lu, F. Xue, H. C. Nie, R. Withers, A. Studer, F. Kremer, N. Narayanan, X. L. Dong, D. H. Yu, L. Q. Chen, Y. Liu, and G. S. Wang, Lead-free (Ag, K) NbO_3 materials for high-performance explosive energy conversion, *Sci. Adv.* **6**, eaba0367 (2020).

- [15] M. Avdeev, J. D. Jorgensen, S. Short, G. A. Samara, E. L. Venturini, P. Yang, and B. Morosin, Pressure induced ferroelectric to antiferroelectric phase transition in $\text{Pb}_{0.99}(\text{Zr}_{0.95}\text{Ti}_{0.05})_{0.98}\text{Nb}_{0.02}\text{O}_3$, *Phys. Rev. B* **73**, 064105 (2006).
- [16] A. Chauhan, S. Patel, S. Wang, N. Novak, B. X. Xu, P. Lv, R. Vaish, and C. S. Lynch, Enhanced performance of ferroelectric materials under hydrostatic pressure, *J. Appl. Phys.* **122**, 224105 (2017).
- [17] S. Patel, A. Chauhan, R. Vaish, and C. S. Lynch, Large barocaloric effect and pressure-mediated electrocaloric effect in $\text{Pb}_{0.99}\text{Nb}_{0.02}(\text{Zr}_{0.95}\text{Ti}_{0.05})_{0.98}\text{O}_3$ ceramics, *J. Am. Ceram. Soc.* **100**, 4902 (2017).
- [18] Z. L. Lu, W. C. Bao, G. Wang, S. K. Sun, L. H. Li, J. L. Li, H. J. Yang, H. F. Ji, A. Feteira, D. J. Li, F. F. Xu, A. K. Kleppe, D. W. Wang, S. Y. Liu, and I. M. Reaney, Mechanism of enhanced energy storage density in AgNbO_3 -based lead-free antiferroelectrics, *Nano Energy* **79**, 105423 (2021).
- [19] N. N. Luo, K. Han, M. J. Cabra, X. Z. Liao, S. J. Zhang, C. Z. Liao, G. Z. Zhang, X. Y. Chen, Q. Feng, J. F. Li, and Y. Z. Wei, Constructing phase boundary in AgNbO_3 antiferroelectrics: pathway simultaneously achieving high energy density and efficiency, *Nat. Commun.* **11**, 4824 (2020).
- [20] N. N. Luo, K. Han, F. P. Zhuo, X. Chao, G. Z. Zhang, L. J. Liu, X. Y. Chen, C. Z. Hu, H. F. Zhou, and Y. Z. Wei, Aliovalent *A*-site engineered AgNbO_3 lead-free antiferroelectric ceramics toward superior energy storage density, *J. Mater. Chem. A* **7**, 14118 (2019).
- [21] J. Wang, Y. Rao, X. H. Fan, J. Zhang, L. Zhao, and K. J. Zhu, Synergic modulation of over-stoichiometrical MnO_2 and SiO_2 -coated particles on the energy storage properties of silver niobate-based ceramics, *Ceram. Int.* **47**, 19595 (2021).
- [22] L. Zhao, Q. Liu, J. Gao, S. J. Zhang, and J. F. Li, Lead-free antiferroelectric silver niobate tantalate with high energy storage performance, *Adv. Mater.* **29**, 1701824 (2017).
- [23] S. Li, H. C. Nie, G. S. Wang, N. T. Liu, M. X. Zhou, F. Cao, and X. L. Dong, Novel AgNbO_3 -based lead-free ceramics featuring excellent pyroelectric properties for infrared detecting and energy-harvesting applications via antiferroelectric/ferroelectric phase-boundary design, *J. Mater. Chem. C* **7**, 4403 (2019).
- [24] D. Fu, M. Itoh, and S. Koshihara, Dielectric, ferroelectric, and piezoelectric behaviors of $\text{AgNbO}_3\text{-KNbO}_3$ solid solution, *J. Appl. Phys.* **106**, 104104 (2009).
- [25] A. Kania, Dielectric properties of $\text{Ag}_{1-x}\text{AxNbO}_3$ (*A*: K, Na and Li) and $\text{AgNb}_{1-x}\text{Ta}_x\text{O}_3$ solid solutions in the vicinity of diffuse phase transitions, *J. Phys. D: Appl. Phys.* **34**, 1447 (2001).
- [26] E. Buixaderas, I. Gregora, J. Hlinka, J. Dec, and T. Lukasiewicz, Raman and IR phonons in ferroelectric $\text{Sr}_{0.35}\text{Ba}_{0.69}\text{Nb}_2\text{O}_{6.04}$ single crystals, *Phase Transitions* **86**, 217 (2013).
- [27] R. J. Zeches *et al.* A strain-driven morphotropic phase boundary in BiFeO_3 , *Science* **326**, 977 (2009).
- [28] M. Yashima, S. Matsuyama, R. Sano, M. Itoh, K. Tsuda, and D. Fu, Structure of ferroelectric silver niobate AgNbO_3 , *Chem. Mater.* **23**, 1643 (2011).
- [29] M. K. Niranjan and S. Asthana, First principles study of lead-free piezoelectric AgNbO_3 and $(\text{Ag}_{1-x}\text{K}_x)\text{NbO}_3$ solid solutions, *Solid State Commun.* **156**, 1707 (2012).
- [30] B. Xu, C. Paillard, B. Dkhil, and L. Bellaiche, Pinched hysteresis loop in defect-free ferroelectric materials, *Phys. Rev. B* **9**, 140101(R) (2016).
- [31] W. W. Ji, B. J. Fang, X. Y. Zhao, S. Zhang, X. L. Lu, and J. N. Ding, Enhancing electrical properties of high-Curie temperature piezoelectric ceramics BNT-PZT and their mechanism, *Curr. Appl. Phys.* **19**, 1367 (2019).
- [32] X. Lv, J. W. Zhang, Y. Liu, F. Li, X. X. Zhang, and J. G. Wu, Synergetic contributions in phase boundary engineering to the piezoelectricity of potassium sodium niobate lead-free piezoceramics, *ACS Appl. Mater. Inter.* **12**, 39455 (2020).
- [33] Z. P. Wang, R. R. Kang, W. Y. Liu, L. X. Zhang, L. Q. He, S. Y. Zhao, H. X. Duan, Z. H. Yu, F. H. Yu, F. Kang, Q. Z. Sun, T. R. Zhang, P. Mao, J. P. Wang, and L. Zhang, $(\text{Bi}_{0.5}\text{Na}_{0.5})\text{TiO}_3$ -based relaxor ferroelectrics with medium permittivity featuring enhanced energy-storage density and excellent thermal stability, *Chem. Eng. J.* **427**, 131989 (2022).
- [34] D. Arney, C. Hardy, B. Greve, and P. A. Maggard, Flux synthesis of AgNbO_3 : Effect of particle surfaces and sizes on photocatalytic activity, *J. Photoch. Photobio. A* **214**, 54 (2010).
- [35] X. He, C. Chen, C. B. Li, H. R. Zeng, and Z. G. Yi, Ferroelectric, photoelectric, and photovoltaic performance of silver niobate ceramics, *Adv. Funct. Mater.* **29**, 1900918 (2019).
- [36] A. W. Xie, R. Z. Zuo, Z. L. Qiao, Z. Q. Fu, T. F. Hu, and L. F. Fei, $\text{NaNbO}_3 - (\text{Bi}_{0.5}\text{Li}_{0.5})\text{TiO}_3$ lead-free relaxor ferroelectric capacitors with superior energy-storage performances via multiple synergistic design, *Adv. Energy Mater.* **11**, 2101378 (2021).
- [37] B. K. Song, H. G. Gu, M. S. Fang, X. G. Chen, H. Jiang, R. Y. Wang, T. Y. Zhai, Y. T. Ho, and S. Y. Liu, Layer-dependent dielectric function of wafer-scale 2D MoS_2 , *Adv. Opt. Mater.* **7**, 1801250 (2019).
- [38] Z. H. Duan, Z. G. Hu, K. Jiang, Y. W. Li, G. S. Wang, X. L. Dong, and J. H. Chu, Temperature-dependent dielectric functions and interband critical points of relaxor lead hafnate-modified $\text{PbSc}_{1/2}\text{Ta}_{1/2}\text{O}_3$ ferroelectric ceramics by spectroscopic ellipsometry, *Appl. Phys. Lett.* **102**, 151908 (2013).
- [39] R. E. Cohen, Origin of ferroelectricity in oxide ferroelectrics and the difference in ferroelectric behavior of BaTiO_3 and PbTiO_3 , *Ferroelectrics* **136**, 65 (1992).
- [40] L. Chen, F. X. Long, H. Qi, H. Liu, S. Q. Deng, and J. Chen, Outstanding energy storage performance in high-hardness $(\text{Bi}_{0.5}\text{K}_{0.5})\text{TiO}_3$ -based lead-free relaxors via multi-scale synergistic design, *Adv. Funct. Mater.* **32**, 2110478 (2021).
- [41] Q. Q. Li, J. Y. Wang, M. J. Li, S. Guo, J. Z. Zhang, Z. G. Hu, Z. Y. Zhou, G. S. Wang, X. L. Dong, and J. H. Chu, Structure evolution mechanism of $\text{Na}_{0.5}\text{Bi}_{2.5}\text{Nb}_2 - x\text{W}_x\text{O}_9 + \delta$ ferroelectric ceramics: Temperature-dependent optical evidence and first-principles calculations, *Phys. Rev. B* **96**, 024101 (2017).

- [42] J. P. Perdew and M. Levy, Physical Content of the Exact Kohn-Sham Orbital Energies: Band Gaps and Derivative Discontinuities, *Phys. Rev. Lett.* **51**, 1884 (1983).
- [43] S. R. Abramson, R. Baer, and L. Kronik, Fundamental and excitation gaps in molecules of relevance for organic photovoltaics from an optimally tuned range-separated hybrid functional, *Phys. Rev. B* **84**, 075144 (2011).
- [44] A. J. Cohen, P. M. Sanchez, and W. Yang, Fractional charge perspective on the band gap in density-functional theory, *Phys. Rev. B* **77**, 155123 (2008).
- [45] X. C. Wang, C. Meng, and Y. Y. Wang, Insight for the construction of R-T phase boundary in KNN piezoceramics from the view of energy band structure and electron density, *Ceram. Int.* **47**, 28500 (2021).
- [46] H. Li, L. Wang, L. Z. Xu, A. P. Li, P. Mao, Q. P. Wu, and Z. Y. Xie, First-principles study on the structural, elastic, piezoelectric and electronic properties of $(\text{BaTiO}_3, \text{LiTaO}_3)$ -modified KNbO_3 , *Mater. Today Commun.* **26**, 102092 (2021).
- [47] Y. Q. Xu, S. Y. Wu, L. N. Wu, L. J. Zhang, and S. Y. Zhong, First-principles investigations on the visible light photocatalytic activity of NaNbO_3 by N and F doping, *Eur. Phys. J. B* **92**, 68 (2019).
- [48] A. Shigemi and T. Wada, Crystallographic phase stabilities and electronic structures in AgNbO_3 by first-principles calculation, *Mol. Simulat.* **34**, 1105 (2008).
- [49] Y. Shiratori, A. Magrez, W. Fischer, C. Pithan, and R. Waser, Temperature-induced phase transitions in micro-, submicro-, and nanocrystalline NaNbO_3 , *J. Phys. Chem. C* **111**, 18493 (2007).
- [50] D. L. Rousseau, R. P. Bauman, and S. P. S. Porto, Normal mode determination in crystals, *J. Raman Spectrosc.* **10**, 253 (1981).
- [51] M. K. Niranjan, K. G. Prasad, S. Asthana, S. Rayprol, and V. Siruguri, Investigation of structural, vibrational and ferroic properties of AgNbO_3 at room temperature using neutron diffraction, Raman scattering and densityfunctional theory, *J. Phys. D: Appl. Phys.* **48**, 215303 (2015).
- [52] L. P. Xu, K. Jiang, J. Z. Zhang, G. S. Xu, Z. G. Hu, and J. H. Hao, Phase transitions and thermotropic phase boundaries in MnO_2 -doped $(\text{K}_{0.5}\text{Na}_{0.5})\text{NbO}_3\text{-}0.05\text{LiNbO}_3$ single crystals: Raman scattering evidence at elevated temperatures, *Appl. Phys. Lett.* **106**, 122901 (2015).
- [53] P. Pruzan, D. Gourdain, and J. C. Chervin, Vibrational dynamics and phase diagram of KNbO_3 up to 30 GPa and from 20 to 500 K, *Phase Transitions* **80**, 1103 (2007).
- [54] C. H. Perry, J. H. Fertel, and T. F. Mcnelly, Temperature dependence of the Raman spectrum of SrTiO_3 and KTaO_3 , *J. Chem. Phys.* **47**, 1619 (1967).
- [55] R. Z. Zuo, H. Qi, J. Fu, J. F. Li, and L. T. Li, Multiscale identification of local tetragonal distortion in $\text{NaNbO}_3 - \text{BaTiO}_3$ weak relaxor ferroelectrics by Raman, synchrotron x-ray diffraction, and absorption spectra, *Appl. Phys. Lett.* **111**, 132901 (2017).
- [56] E. Husson, Raman spectroscopy applied to the study of phase transitions, *Key. Eng. Mater.* **155**, 1 (1998).
- [57] Z. H. Dai, D. Y. Li, Z. J. Zhou, S. Zhou, W. G. Liu, J. J. Liu, X. Wang, and X. B. Ren, A strategy for high performance of energy storage and transparency in KNN-based ferroelectric sceramics, *Chem. Eng. J.* **427**, 131959 (2022).
- [58] P. Lautenschlager, M. Garriga, S. Logothetidis, and M. Cardona, Interband critical points of GaAs and their temperature dependence, *Phys. Rev. B* **35**, 9174 (1987).
- [59] B. Mihailova, N. Waesemann, B. J. Maier, A. M. Welsch, R. J. Angel, and U. Bismayer, Pressure-induced structural transformations in advanced ferroelectrics with relaxor behavior, *High Press. Res.* **33**, 595 (2013).
- [60] I. J. Fritz and J. D. Keck, Pressure-temperature phase diagrams for several modified lead zirconate ceramics, *J. Phys. Chem. Solids* **39**, 1163 (1978).